PAPER

New insight into rare-earth doped gadolinium molybdate nanophosphor assisted broad spectral converters from UV to NIR for silicon solar cells†

Pawan Kumar[ab] and Bipin Kumar Gupta*[a]

We have successfully synthesized rare-earth doped gadolinium molybdate $Gd_2(MoO_4)_3{:}Re^{3+}$ ($Re^{3+} = Eu^{3+}$, Tb^{3+}, Tm^{3+} and Er^{3+}/Yb^{3+}) nanophosphors for solar cell application as a broad spectral converter from the ultraviolet (UV) to the near infrared (NIR) regions in a single host lattice using a facile solid state reaction method. The gross structure, surface morphology and microstructure of these nanophosphors have been investigated by X-ray powder diffraction (XRD), scanning electron microscopy (SEM) and transmission/high-resolution transmission electron microscopy (TEM/HRTEM) techniques , respectively. Photoluminescence (PL) and time-resolved photoluminescence (TRPL) spectroscopic methods have been used to explore the striking luminescence properties of the synthesized nanophosphors. The $Gd_2(MoO_4)_3{:}Eu^{3+}$ nanophosphor exhibits a hypersensitive red emission (616 nm) at an excitation wavelength in the range of 250–475 nm corresponding to a $^5D_0-^7F_2$ transition. The $Gd_2(MoO_4)_3{:}Tb^{3+}$ and $Gd_2(MoO_4)_3{:}Tm^{3+}$ nanophosphors demonstrate a strong green emission at 541 nm and a deep blue emission at 453 nm upon an excitation wavelength of 378 nm and 266 nm, respectively. Moreover, the upconversion characteristic of the $Gd_2(MoO_4)_3{:}Er^{3+}/Yb^{3+}$ nanophosphor exhibits strong green emission at 545 nm and red emission at 657 nm corresponding to $^4S_{3/2}-^4I_{15/2}$ and $^4F_{9/2}-^4I_{15/2}$ transitions respectively. Furthermore, the $Gd_2(MoO_4)_3{:}Er^{3+}/Yb^{3+}$ upconversion nanophosphor emits in the NIR spectrum region at 994 nm upon a 980 nm excitation wavelength. Hence, the obtained PL emission results with a lifetime in milliseconds reveal that these nanophosphors could be futuristic promising broad spectral converter phosphors which may possibly integrate with the next-generation Si-solar cell to enhance the efficiency of the cell.

1. Introduction

Energy is directly related to the currency of any country. There is no doubt that it is always in huge demand, but unluckily, it is always in short supply which is insufficient to match the unparalleled population explosion and our changing comfort lifestyle. Undeniably, we are facing an energy crisis and it has become the most important commodity. Energy consumption will have almost doubled by 2050 compared to the energy consumption in 2001.[1,2] Consequently, renewable energy sources that can provide sufficient energy to meet the worldwide energy demand have attained huge attention.[1–5] Sunlight is the most important renewable source of energy which can be directly converted into heat and electricity. Moreover, sunlight is a plentiful source of energy; available almost everywhere in

the world without any cost.[5] The photovoltaic cells which convert sunlight directly into electricity are the most prominent source of renewable energy. However, photovoltaic cells are only contributing a limited portion of the energy demand. Therefore, over the past few decades, significant effort has been directed to the development of efficient photovoltaic cells. Still, the efficient and economic cost conversion of sunlight into electricity remains a challenging task.[6–8] Commercial availability and the economic approach of crystalline and polycrystalline solar cells have been dominating the photovoltaic market to date.[9,10] Therefore, an immense amount of research has been devoted to the development of efficient and low cost crystalline and poly-crystalline solar cells in the past few decades.

A major drawback of Si-solar cells is that they don't utilize the full solar spectrum when sunlight falls on their surface which limits the energy conversion efficiency. It is well established that the solar spectrum has photons ranging from 250–2500 nm (ultraviolet to infrared) at air mass 1.5 global (AM 1.5G). But, photovoltaic cells only utilize a small portion of the solar spectrum which is attributed only to photons that match the band gap of the material.[11] In general; there are two kinds of loss in solar cells which limit their efficiency. One is

[a]CSIR – National Physical Laboratory, Dr K S Krishnan Road, New Delhi, 110012, India. E-mail: bipinbhu@yahoo.com; Fax: +91-11-45609310; Tel: +91-11-45609385

[b]Academy of Scientific and Innovative Research (AcSIR), CSIR – National Physical Laboratory, New Delhi – 110012, India

that the photons with an energy higher than the band gap (UV radiations) are not efficiently used; the excess energy of the photons is dissipated in the form of heat. Secondly, the photons with low energy (IR radiation) are not absorbed by solar cells and these are transmitted. It is observed that the 70% loss in solar cells is related to these losses, known as spectral mismatch. One of the promising ways to address this issue is by using downshift (DS) or upconversion (UC) materials as a spectral converter to minimise these losses (thermalisation and non-absorbed losses). A downshift material can absorb the photons with high energy and emit photons that have a lower energy in the visible spectrum region which are subsequently absorbed by the solar cell without any heat dissipation. Upconversion materials absorb two photons that have an energy less than that of the band gap of the solar cell and are converted into a utilized photon (having energy in the visible spectrum region) which is absorbed by the solar cell. This approach to minimising the thermalisation and non-absorbed losses by applying a luminescent layer on the solar cell is termed as third generation solar conversion.[5] Although there are many materials that have been proposed as luminescence concentrators for the enhancement of solar cell efficiency, lanthanide doped materials are the most suitable materials for solar spectral converters due to their electron rich energy level structure which offers a superficial photon management. Therefore, significant effort has been dedicated to the enhancement of the efficiency of solar cells *via* modification of the solar spectrum using trivalent lanthanide doped materials.[12–23]

Among the various trivalent lanthanide ions (Ln^{3+}), materials doped with Eu^{3+}/Er^{3+} ions (downshift/upconversion phosphors) have gained more inquisitiveness as spectral converters. These materials can emit photons in the visible spectrum which are useful in solar cell applications to create electron–hole pairs. Moreover, host lattices containing d-block transition elements (like tungstate and molybdate) have an advantage over other host lattices because the excitation band is broad due to the charge transfer (CT) in the O–Mo or O–W bond occurring in the UV region, which is sufficiently transferred to the trivalent lanthanide ion.[24] Furthermore, the $Gd_2(MoO_4)_3$ host matrix possesses beneficial properties such as a high refractive index, high thermal stability, low toxicity and high photochemical stability.

In the present investigation, we have synthesized $Gd_2(MoO_4)_3$:Re^{3+} (Re^{3+} = Eu^{3+}, Tb^{3+}, Tm^{3+} and Er^{3+}/Yb^{3+}) nanophosphors for a proposed solar cell application where these nanophosphors act as a spectral converter nanophosphor. These nanophosphors have the capability to absorb light in a broad range from UV to IR and can emit red, green and blue emission in the visible and NIR regions. The $Gd_2(MoO_4)_3$:Eu^{3+} downshift nanophosphor demonstrates a photoluminescence emission peak at 616 nm (hypersensitive red emission) upon broad excitation ranging from 250–475 nm. Moreover, other two downshift nanophosphors $Gd_2(MoO_4)_3$:Tb^{3+} and $Gd_2(MoO_4)_3$:Tm^{3+} exhibit the emission peaks at 541 nm (strong green) and 453 nm (deep blue) respectively. Furthermore, the $Gd_2(MoO_4)_3$:Er^{3+}/Yb^{3+} upconversion nanophosphor shows strong green emission at 545 nm and red emission at 657 nm.

Additionally, the $Gd_2(MoO_4)_3$:Er^{3+}/Yb^{3+} upconversion nanophosphor exhibits emission at 994 nm (NIR region) upon a 980 nm excitation wavelength, which is rarely reported in the literature.[25,26] Thus, $Gd_2(MoO_4)_3$:Re^{3+} (Re^{3+}, Eu^{3+}, Tb^{3+}, Tm^{3+} and Er^{3+}/Yb^{3+}) nanophosphors could be efficiently used as spectral converters, which can absorb light in the 250–475 nm/NIR spectrum region and emit in the visible and NIR region which is highly desirable for the modification of the Si-solar cell spectrum. Hence, the obtained results provide a new podium of $Gd_2(MoO_4)_3$:Re^{3+} (Re^{3+}, Eu^{3+}, Tb^{3+}, Tm^{3+} and Er^{3+}/Yb^{3+}) nanophosphors to examine their interesting photoluminescence properties in detail for a proposed Si-solar cell application.

2. Experimental

2.1 Materials

The precursors; Y_2O_3 (99.99%), Eu_2O_3 (99.99%), Tm_2O_3 (99.99%), Tb_4O_7 (99.99%), $Er(NO_3)_3 \cdot 5H_2O$ (99.99%), Yb_2O_3 (99.99%) and $(NH_4)_6Mo_7O_{24} \cdot 4H_2O$ (AR grade, 99%) were purchased from Sigma-Aldrich. All reagents were of analytical (AR) grade and used as received without further purification.

2.2 Synthesis of $Gd_2(MoO_4)_3$:Re^{3+} (Re^{3+}, Eu^{3+}, Tb^{3+}, Tm^{3+} and Er^{3+}/Yb^{3+}) nanophosphors

A facile solid state reaction was used for the synthesis of $Gd_2(MoO_4)_3$:Re^{3+} (Re^{3+}, Eu^{3+}, Tb^{3+}, Tm^{3+} and Er^{3+}/Yb^{3+}) which can be easily scaled-up for large quantities. In order to optimize the concentration and temperature, first we synthesized the red emitting $Gd_{2-x}(MoO_4)_3$:Eu_x^{3+} (x = 0.1 to 0.5) nanophosphor using a solid state reaction method. According to the stoichiometric ratio, the starting materials Gd_2O_3, Eu_2O_3, and $(NH_4)_6Mo_7O_{24} \cdot 4H_2O$ were taken. After precise weighing of these materials, the materials were appropriately crushed in an agate mortar for homogeneous mixing. The homogeneous mixture was kept in an alumina crucible and heated in a box furnace at a temperature of 1000 °C for 3 h. The doping concentration of Eu^{3+} was varied (x = 0.1 to 0.5) in order to attain the optimum dopant concentration for the strongest red emission and it was observed that x = 0.2 is the optimum concentration. Furthermore, in order to compare the luminescence intensity with sintering temperature, the $Gd_{1.8}(MoO_4)_3$:$Eu_{0.2}^{3+}$ phosphor was heated at 800 °C, 900 °C, 1000 °C and 1100 °C. The green and blue nanophosphors were synthesized by doping with different rare-earth ions (Tb^{3+} and Tm^{3+}). The nanophosphor was doped with Tb^{3+} ions were doped to achieve the green emission and Tm^{3+} ions for blue emission. Similarly, the $Gd_2(MoO_4)_3$:Er^{3+}/Yb^{3+} (Er^{3+} = 5 mol% and Yb^{3+} = 10 mol%) upconversion nanophosphor were also synthesized by a solid state reaction method keeping the same conditions as for the downshift nanophosphors. Using this method, the yield of the materials was more than 90% in all cases (downshift and upconversion nanophosphors) with a high degree of homogeneity throughout the mass. The versatility of this method is such that one could easily synthesize large quantities of homogeneous rare earth doped nanophosphors with a narrow size distribution.

2.3 Characterization

The crystal structure was investigated using X-ray powder diffraction (XRD) with a Bruker AXS D8 Advance X-ray diffractometer, using Cu Kα_1 radiation (λ = 1.5406 Å). The surface morphology was studied using Carl ZEISS EVOR-18 equipment at a 10 kV operating voltage. Transmission electron microscopy (TEM) and high-resolution transmission electron microscopy (HRTEM) micrographs were recorded using a Tecnai G2 S-Twin transmission electron microscope with a field emission gun operating at 300 kV. An Edinburgh spectrometer was used for photoluminescence (PL) and time-resolved photoluminescence (TRPL) spectroscopy, where a xenon lamp acted as the source of excitation. To estimate the absolute luminescence quantum efficiency of the QC phosphors, an integrating sphere equipped with an Edinburgh spectrometer (model F900) instrument was used, and then the integrated fractions of luminous flux and radiant flux were measured using the standard method; quantum efficiency was evaluated. The NIR PL emission and PL mapping of the nanophosphors was performed using a WITech alpha 300R+ confocal PL microscope system, where 375 and 980 nm diode lasers act as source of excitations.

3. Results and discussion

A facile solid state reaction method has been used to synthesize Gd$_2$(MoO$_4$)$_3$:Re^{3+} (Re^{3+}, Eu^{3+}, Tb^{3+}, Tm^{3+} and Er^{3+}/Yb^{3+}). The X-ray diffraction (XRD) technique has been carried out to investigate the gross structure and phase purity of the nanophosphors. The XRD pattern of the Gd$_{1.8}$(MoO$_4$)$_3$:Eu$_{0.2}$$^{3+}$ downshift nanophosphor is illustrated in Fig. 1(a). The XRD result reveals that the nanophosphor has an orthorhombic crystalline structure with space group Pba2. The estimated lattice parameters for the Gd$_{1.8}$(MoO$_4$)$_3$:Eu$_{0.2}$$^{3+}$ nanophosphor are a = (10.1631 ± 0.0023) Å, b = (10.1132 ± 0.0021) Å and c = (10.74 ± 0.0027) Å, which are comparable with the existing Gd$_2$(MoO$_4$)$_3$ host (JCPDS card no. 20-0408). The estimated crystallite size of the Gd$_{1.8}$(MoO$_4$)$_3$:Eu$_{0.2}$$^{3+}$ nanophosphor is ~28 nm using the standard Scherrer formula. The XRD patterns of Gd$_{2-x}$(MoO$_4$)$_3$:Eu$_x$$^{3+}$ downshift nanophosphors for different concentrations (x = 0.1 to 0.5) are demonstrated in Fig. S1 (see ESI†). The lattice parameters for all variants of the Gd$_{2-x}$(MoO$_4$)$_3$:Eu$_x$$^{3+}$ nanophosphors (x = 0.1 to 0.5) were calculated from the observed d-values through a least square fitting
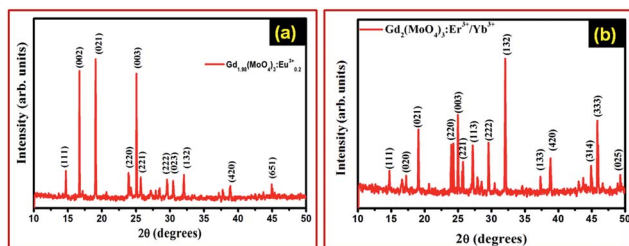
method using computer program based unit cell refinement software.[27] The unit cell volume was estimated from these parameters and is exhibited in Table S1.† It was observed that the unit cell volume increased with Eu^{3+}-doping concentration up to a value of 0.2 and then after this it started to decrease. The decrease in the unit cell volume decreases the inter-ionic distance between the Eu^{3+} ions which leads to an increase in non-radiative emission which decreases the luminescence intensity. Furthermore, the obtained results for the different concentrations (x = 0.1 to 0.5) of Gd$_{2-x}$(MoO$_4$)$_3$:Eu$_x$$^{3+}$ nanophosphors, with their unit cell parameters, are consistent with the obtained PL emission results. Therefore, the emission intensity is maximum for doping concentration x = 0.2. Fig. S2† exhibits the XRD patterns of the Gd$_{1.8}$(MoO$_4$)$_3$:Eu$_{0.2}$$^{3+}$ downshift nanophosphor at different sintering temperatures (800 °C, 900 °C, 1000 °C and 1100 °C).[28] The obtained XRD patterns of the Gd$_{1.8}$(MoO$_4$)$_3$:Eu$_{0.2}$$^{3+}$ nanophosphor at different sintering temperatures reveals that the relative peak intensity of Gd$_{1.8}$(MoO$_4$)$_3$:Eu$_{0.2}$$^{3+}$ increases when the sintering temperature increases from 800 to 1000 °C. Above 1000 °C, the secondary phases start to appear, and as a result it affects the PL intensity of the Gd$_{1.8}$(MoO$_4$)$_3$:Eu$_{0.2}$$^{3+}$ nanophosphor, which is further discussed in detail in the PL section. Fig. 1(b) demonstrates the XRD pattern of the Gd$_2$(MoO$_4$)$_3$:Er^{3+}/Yb^{3+} upconversion nanophosphor. The XRD patterns of the Gd$_{1.8}$(MoO$_4$)$_3$:Tb$_{0.2}$$^{3+}$ and Gd$_{1.8}$(MoO$_4$)$_3$:Tm$_{0.2}$$^{3+}$ downshift nanophosphors are illustrated in Fig. S3 (see ESI†).

Scanning electron microscopy (SEM) has been used to explore the surface morphology of the synthesized nanophosphors. Fig. 2(a) exhibits the SEM image of the Gd$_{1.8}$(MoO$_4$)$_3$:Eu$_{0.2}$$^{3+}$ downshift nanophosphor. To gain more information about the microstructure of the Gd$_{1.8}$(MoO$_4$)$_3$:Eu$_{0.2}$$^{3+}$ nanophosphor, transmission electron microscopy (TEM) and
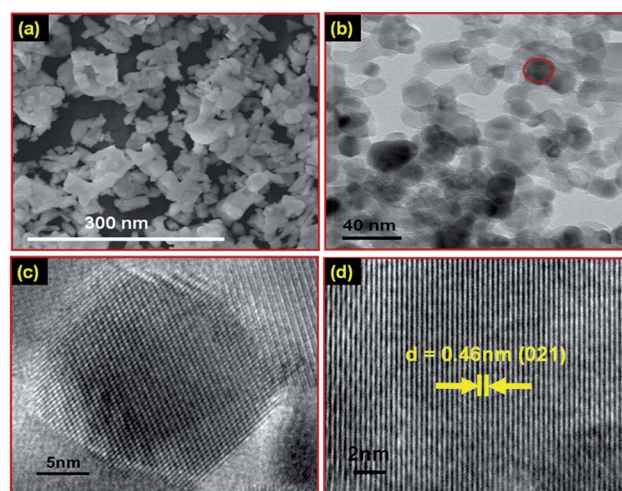

Fig. 2 (a) SEM image of the Gd$_{1.8}$(MoO$_4$)$_3$:Eu$_{0.2}$$^{3+}$ downshift nanophosphor, (b) TEM image of the Gd$_{1.8}$(MoO$_4$)$_3$:Eu$_{0.2}$$^{3+}$ downshift nanophosphor, (c) a typical HRTEM image of a selected individual particle which is marked by the red circle in (b), and (d) HRTEM image of the Gd$_{1.8}$(MoO$_4$)$_3$:Eu$_{0.2}$$^{3+}$ downshift nanophosphor which exhibits the clear lattice fringes without any distortion.

Fig. 1 The XRD patterns of the (a) Gd$_{1.8}$(MoO$_4$)$_3$:Eu$_{0.2}$$^{3+}$ downshift nanophosphor and (b) Gd$_2$(MoO$_4$)$_3$:Er^{3+}/Yb^{3+} upconversion nanophosphor.

high-resolution transmission electron microscopy (HRTEM) was performed. The TEM image of the $Gd_{1.8}(MoO_4)_3:Eu_{0.2}^{3+}$ downshift nanophosphor is shown in Fig. 2(b). The TEM image shows that the average particle size of the nanophosphor is ~24 nm. The size distribution histogram of the $Gd_{1.8}(MoO_4)_3:Eu_{0.2}^{3+}$ downshift nanophosphor is shown in Fig. S4 (see ESI†). The HRTEM image of a selected individual nanoparticle (marked in Fig. 2(b)) is shown in Fig. 2(c). Fig. 2(d) represents that the HRTEM image of the nanophosphor exhibits the clear lattice fringes without any distortion, which confirms that the nanophosphor has good crystal quality. The estimated d-spacing is measured to be ~0.46 nm from Fig. 2(d), which is analogous to the d-spacing corresponding to the (021) plane (JCPDS card no. 20-0408). Moreover, the selected area electron diffraction (SAED) pattern of the $Gd_{1.8}(MoO_4)_3:Eu_{0.2}^{3+}$ nanophosphor was also obtained. Fig. S5 (see ESI†) demonstrates the SAED pattern of $Gd_{1.8}(MoO_4)_3:Eu_{0.2}^{3+}$ which clearly exhibits that the nanophosphor is highly crystalline. Furthermore, energy dispersive X-ray analysis (EDAX) was performed for elemental detection. Fig. S6 (see ESI†) shows the EDAX spectrum of the $Gd_2(MoO_4)_3:Eu_{0.2}^{3+}$ downshift nanophosphor which confirms the presence of Gd, Mo, O and Eu. Moreover, the elemental analysis for the upconversion nanophosphor was also performed. The EDAX spectrum of the $Gd_2(MoO_4)_3:Er^{3+}/Yb^{3+}$ upconversion nanophosphor is shown in Fig. S7 (see ESI†) which confirms the presence of Gd, Mo, O, Er and Yb.

Furthermore, PL and TRPL spectroscopy have been carried out to explore the spectroscopic characteristics of the synthesized nanophosphor to examine the feasibility of the nanophosphor for the proposed spectral converter application. The photoluminescence excitation (PLE) spectrum of the $Gd_{1.8}(MoO_4)_3:Eu_{0.2}^{3+}$ downshift nanophosphor is illustrated in

Fig. 3(a). The excitation spectrum has a broad band around 290 nm and sharp peaks in the range of 350–475 nm. The broad band at ~290 nm is due to the energy charge transfer between Mo–O. It is well known that a transition metal containing host matrix (like VO_4^{3-}, NbO_4^{3-}, WO_4^{2-} and MoO_4^{2-} group containing host matrices) has an additional advantage over the other host matrices as it can absorb a broad range in the UV spectrum region due to the charge transfer between the electron deficient transition metal ion and electron rich oxygen ion.[24,29] Therefore, the energy transfer between the transition metal atom and the oxygen atom is a very important factor to enhance the luminescence properties of inorganic phosphors. The sharp peaks are characteristics of the f–f transition within the $4f^6$ electron shell of the Eu^{3+} ion in the host lattices. The two strong excitation peaks at 395 nm and 465 nm are attributed to the $^7F_0-^5L_6$ and $^7F_0-^5D_2$ transitions of the Eu^{3+} ion, respectively.[30] Fig. 3(b) depicts the emission spectrum of the $Gd_{1.8}(MoO_4)_3:Eu_{0.2}^{3+}$ downshift nanophosphor at an excitation wavelength of 395 nm. The emission spectrum shows hyperfine red emission at 616 nm with a quantum efficiency of ~84%. The emission peaks at 589 nm, 596 nm, 616 nm, 623 nm and 701 nm are attributed to $^5D_0-^7F_1$, $^5D_0-^7F_1$, $^5D_0-^7F_2$, $^5D_0-^7F_2$ and $^5D_0-^7F_4$ transitions, respectively. The strong red emission of the nanophosphor has been obtained by optimising the doping concentration of Eu^{3+} ions. Fig. 3(c) reveals the variation in luminescence intensity with the doping concentration of Eu^{3+} ions. It has been observed that the luminescence intensity increases with an increase in the doping concentration of Eu^{3+} up to 10 mol%. However, with a further increase of Eu^{3+} concentration, the luminescence intensity starts to decrease and it decreases rapidly after 20 mol% concentration. The decrease in luminescence intensity with an increase in Eu^{3+} concentration is due to the decrease in the distance between two Eu^{3+} ions in the host matrix. This decrease in the distance between the Eu^{3+} ions reduces the probability of the radiative transitions of the Eu^{3+} ions due to mutual interaction at the shortened distances between two Eu^{3+} ions at high doping concentrations which leads to non-radiative emission which decreases luminescence intensity. Therefore, the obtained result suggests that 10 mol% is the optimised doping concentration. In addition, the $Gd_{1.8}(MoO_4)_3:Eu_{0.2}^{3+}$ nanophosphor has been sintered at different temperatures (800 to 1100 °C) for optimization of the sintering temperature for luminescence intensity. The variation in luminescence intensity with sintering temperature is shown in Fig. S8 (see ESI†). It has been observed that 1000 °C is the optimum temperature having the highest luminescence intensity. Furthermore, the PL emission intensity of the $Gd_{1.8}(MoO_4)_3:Eu_{0.2}^{3+}$ downshift nanophosphor decreases at 1100 °C and above. The decrease in PL emission intensity at 1100 °C is due to the formation of secondary phases at high temperatures which was earlier observed in the XRD pattern of the $Gd_{1.8}(MoO_4)_3:Eu_{0.2}^{3+}$ downshift nanophosphor at 1100 °C. Fig. 3(d) exhibits the emission spectra of the $Gd_{1.8}(MoO_4)_3:Eu_{0.2}^{3+}$ downshift nanophosphor at different excitation wavelengths. It shows that a 395 nm excitation wavelength has the maximum emission intensity which signifies that 395 nm is the prominent excitation wavelength for a maximum emission
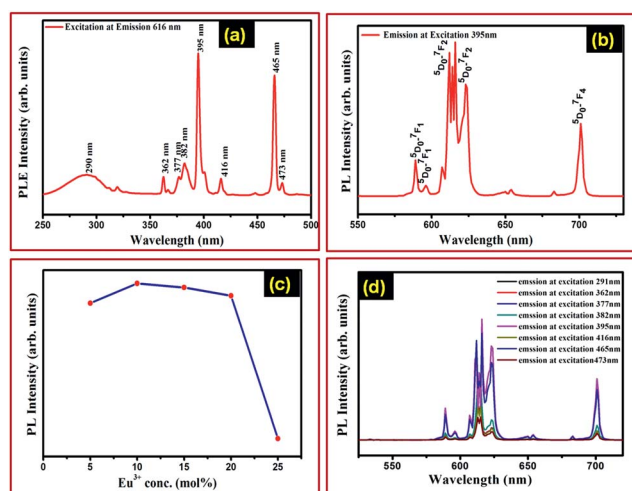

Fig. 3 (a) The excitation spectrum of the $Gd_{1.8}(MoO_4)_3:Eu_{0.2}^{3+}$ downshift nanophosphor at emission 616 nm, (b) the PL emission spectrum with quantum efficiency ~84% of the $Gd_{1.8}(MoO_4)_3:Eu_{0.2}^{3+}$ downshift nanophosphor at an excitation wavelength of 395 nm, (c) PL intensity variation with doping concentration of Eu^{3+} in the $Gd_{2-x}(MoO_4)_3:Eu_x^{3+}$ downshift nanophosphor and (d) PL emission spectra of the $Gd_{1.8}(MoO_4)_3:Eu_{0.2}^{3+}$ downshift nanophosphor at different excitation wavelengths.

intensity. The proposed energy level diagram for the $Gd_{1.8}$-$(MoO_4)_3$:$Eu_{0.2}^{3+}$ downshift nanophosphor has been illustrated in Fig. S9 (see ESI†) which explicated the downshift mechanism for the luminescence process in the $Gd_{1.8}(MoO_4)_3$:$Eu_{0.2}^{3+}$ nanophosphor.

Moreover, the photoluminescence properties of the $Gd_{1.8}$-$(MoO_4)_3$:$Tb_{0.2}^{3+}$ and $Gd_{1.8}(MoO_4)_3$:$Tm_{0.2}^{3+}$ downshift nanophosphors have also been carried out to explore the spectroscopic characteristics of the synthesized nanophosphors to examine the feasibility of these nanophosphors with different dopants for possible spectral converter application. Fig. S10 (see ESI†) exhibits the photoluminescence properties of the $Gd_{1.8}$-$(MoO_4)_3$:$Tb_{0.2}^{3+}$ and $Gd_{1.8}(MoO_4)_3$:$Tm_{0.2}^{3+}$ downshift nanophosphors. Fig. S10(a)† shows that the emission spectrum of the $Gd_{1.8}(MoO_4)_3$:$Tb_{0.2}^{3+}$ downshift nanophosphor has strong green emission at 541 nm upon excitation at 378 nm. Fig. S10(b)† shows the excitation spectrum of the $Gd_{1.8}$-$(MoO_4)_3$:$Tb_{0.2}^{3+}$ downshift nanophosphors at emission of 541 nm. The emission spectrum of the $Gd_{1.8}(MoO_4)_3$:$Tm_{0.2}^{3+}$ downshift nanophosphor is illustrated in Fig. S11(c).† The emission spectrum of the $Gd_{1.8}(MoO_4)_3$:$Tm_{0.2}^{3+}$ downshift nanophosphor shows hypersensitive blue emission at 453 nm upon excitation at 266 nm. Fig. S10(d)† shows the excitation spectrum of the $Gd_{1.8}(MoO_4)_3$:$Tm_{0.2}^{3+}$ downshift nanophosphor at emission of 453 nm. The TRPL technique is an imperative and non-destructive tool which has been used to determine the decay lifetime of the nanophosphor. The lifetime data of a nanophosphor is very important and it helps to decide a suitable application for the nanophosphor. Fig. S11(a) (see ESI†) shows the decay profile of the $Gd_{1.8}(MoO_4)_3$:$Eu_{0.2}^{3+}$ downshift nanophosphor at emission of 616 nm upon an excitation wavelength of 395 nm for $^7F_0$–$^5D_2$ transitions of Eu^{3+} ions. The inset in Fig. S11(a)† exhibits the exponential fitting parameters of the decay profile of the $Gd_{1.8}(MoO_4)_3$:$Eu_{0.2}^{3+}$ downshift nanophosphor. The decay profile has been best fitted to the double exponential function as described in eqn (1):[31]

$$I(t) = A_1 \exp(-t/\tau_1) + A_2 \exp(-t/\tau_2) \quad (1)$$

where τ_1, τ_2, A_1 and A_2 are the decay lifetimes of the luminescence and weighting parameters, respectively.

The obtained parameters after the double exponential fitting are listed in the inset of Fig. S11(a).† The decay lifetimes of the $Gd_{1.8}(MoO_4)_3$:$Eu_{0.2}^{3+}$ downshift nanophosphor are $\tau_1 \sim 0.56$ ms and $\tau_2 \sim 0.81$ ms. The average decay lifetime of the $Gd_{1.8}$-$(MoO_4)_3$:$Eu_{0.2}^{3+}$ nanophosphor is $\tau_{av} \sim 0.64$ ms which is measured using eqn (2) as described below.

$$\tau_{av} = (A_1\tau_1^2 + A_2\tau_2^2)/(A_1\tau_1 + A_2\tau_2) \quad (2)$$

Therefore, the achieved PL and TRPL results suggest that the $Gd_{1.8}(MoO_4)_3$:$Re_{0.2}^{3+}$ (Re^{3+} = Eu^{3+}, Tb^{3+} and Tm^{3+}) downshift nanophosphors meets the stringent criteria of Si-solar cells and it is highly suitable for Si-solar cells as well as other display and biological applications. The CIE colour co-ordinates of $Gd_{1.8}$-$(MoO_4)_3$:$Re_{0.2}^{3+}$ (Re^{3+} = Eu^{3+}, Tb^{3+} and Tm^{3+}) are exhibited in Fig. S11(b) (see ESI†). The symbolic marks A ($x = 0.66, y = 0.33$),

B ($x = 0.34, y = 0.60$) and C ($x = 0.14, y = 0.11$) demonstrate the CIE colour co-ordinates for $Gd_{1.8}(MoO_4)_3$:$Eu_{0.2}^{3+}$, $Gd_{1.8}$-$(MoO_4)_3$:$Tb_{0.2}^{3+}$ and $Gd_{1.8}(MoO_4)_3$:$Tm_{0.2}^{3+}$ emission, respectively.

In order to explore the upconversion nature of the Gd_2-$(MoO_4)_3$:Er^{3+}/Yb^{3+} nanophosphor, we have also performed PL spectroscopy of the synthesized upconversion nanophosphor. Conceptually, upconversion is a process in which the consecutive absorption of two photons of lower energy (IR spectrum region) and emission of a higher energy photon (visible spectrum region) occurs.[32] Upconversion materials are of particular interest for solar cell application because these materials utilize the IR region of the solar spectrum which is transmitted by solar cells.[15,33–38] The emission spectra of the $Gd_2(MoO_4)_3$:Er^{3+}/Yb^{3+} upconversion nanophosphor upon excitation at a wavelength of 980 nm are shown in Fig. 4(a) and (b). Fig. 4(a) exhibits the strong green emission at 545 nm and red emission at 657 nm, which are attributed to $^4S_{3/2}$–$^4I_{15/2}$ and $^4F_{9/2}$–$^4I_{15/2}$ transitions, respectively. Additionally, the emission spectrum also demonstrates a weak emission centred at a wavelength of 525 nm which is attributed to the $^2H_{11/2}$–$^4I_{15/2}$ transition. Moreover, the $Gd_2(MoO_4)_3$:Er^{3+}/Yb^{3+} upconversion nanophosphor has a strong emission at 994 nm, as shown in Fig. 4(b), which is rarely reported in the literature to the best of our knowledge. This emission is also efficiently contributing to the enhancement of the solar cell efficiency because of the fact that the energy of these photons is very near to that of the band gap of the solar cell. The CIE colour co-ordinates of the $Gd_2(MoO_4)_3$:Er^{3+}/Yb^{3+} nanophosphor corresponding to upconversion emission at 980 nm excitation wavelength are exhibited in Fig. 4(c) with values $x = 0.29$ and $y = 0.68$.

Fig. 4(d) is a schematic diagram for the upconversion process in the $Gd_2(MoO_4)_3$:Er^{3+}/Yb^{3+} nanophosphor. In the

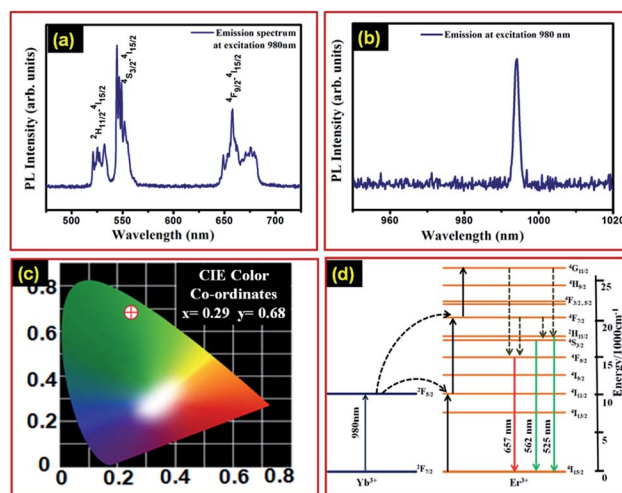**Fig. 4** (a and b) The emission spectra (range 450–750 and 900–1020 nm) of the $Gd_2(MoO_4)_3$:Er^{3+}/Yb^{3+} upconversion nanophosphor at excitation of wavelength 980 nm, (c) the CIE colour coordinates of the $Gd_2(MoO_4)_3$:Er^+/Yb^{3+} upconversion nanophosphor which exhibits a green emission and (d) the schematic for the proposed upconversion process in the $Gd_2(MoO_4)_3$:Er^{3+}/Yb^{3+} nanophosphor.

$Gd_2(MoO_4)_3$:Er^{3+}/Yb^{3+} upconversion nanophosphor, the Yb^{3+} ion acts as a sensitizer and Er^{3+} is used as the dopant, which provides the emission. Yb^{3+} is used for the sensitizer because it can absorb broadly in the NIR region as compared to the Er^{3+} ion. In the case of upconversion, both Yb^{3+} and Er^{3+} ions absorbed incident photons of 980 nm in wavelength.

However, absorption across the $^2F_{7/2}$–$^2F_{5/2}$ transition in Yb^{3+} ions involves more photons compared to absorption across the $^4I_{15/2}$–$^4I_{11/2}$ transition in the case of Er^{3+} ions. Therefore, Yb^{3+} ions absorb most of the incident photons. Furthermore, Yb^{3+} ions can also sufficiently transfer energy to Er^{3+} ions because the energy of the $^2F_{5/2}$ level in Yb^{3+} ions is similar to the energy of the $^4I_{11/2}$ level of the Er^{3+} ions.[30] The excited Yb^{3+} ions relax to the ground state and transfer energy to neighbouring Er^{3+} ions. Therefore, the excited Er^{3+} ions absorb energy from Yb^{3+} ions and are promoted to a higher excitation state which increases the population in a higher energy state. Otherwise, Er^{3+} ions can absorb two low energy photons simultaneously which drives Er^{3+} ions to a higher energy states. The relaxation of the excited Er^{3+} ions to the ground state produces upconversion and emits a strong green coloured emission corresponding to a $^4S_{3/2}$–$^4I_{15/2}$ transition whereas red emission is seen in the case of a $^4F_{9/2}$–$^4I_{15/2}$ transition.

Furthermore, the PL emissions of the $Gd_2(MO_4)_3$:Eu^{3+} and $Gd_2(MoO_4)_3$:Er^{3+}/Yb^{3+} nanophosphors are also comparable with other similar host systems with the same dopants ($GdPO_4$:Eu^{3+}, $GdBO_3$:Eu^{3+}, $GdPO_4$:Er^{3+}/Yb^{3+} and $GdBO_3$:Er^{3+}/Yb^{3+}). Fig. S12(a) (see ESI†) shows the emission spectra of $Gd_2(MO_4)_3$:Eu^{3+}, $GdPO_4$:Eu^{3+} and $GdBO_3$:Eu^{3+} downshift nanophosphors under an excitation wavelength of 395 nm. Fig. S12(b) (see ESI†) exhibits the emission spectra of $Gd_2(MoO_4)_3$:Er^{3+}/Yb^{3+}, $GdPO_4$:Er^{3+}/Yb^{3+} and $GdBO_3$:Er^{3+}/Yb^{3+} upconversion nanophosphors at an excitation wavelength of 980 nm. The obtained results shown in Fig. S12† reveal that a $Gd_2(MO_4)_3$ host lattice based nanophosphor has high emission in both downshift as well as upconversion forms which may be due to an efficient energy transfer from the host lattice to the activator compared to other similar host lattice systems.

Moreover, PL mapping of downshift as well as upconversion nanophosphors was performed for confirmation of uniform emission from the nanophosphors. Fig. 5(a) exhibits the optical image of the $Gd_{1.8}(MoO_4)_3$:$Eu_{0.2}{}^{3+}$ downshift nanophosphor on a glass slide. The PL map of the red marked area in optical image Fig. 5(a) under an excitation wavelength of 375 nm is shown in Fig. 5(b). Fig. 5(b) clearly shows that the nanophosphor has uniform PL emission. The optical image of the $Gd_2(MoO_4)_3$:Er^{3+}/Yb^{3+} upconversion nanophosphor is illustrated in Fig. 5(c). Fig. 5(d) reveals the PL mapping image of the $Gd_2(MoO_4)_3$:Er^{3+}/Yb^{3+} upconversion nanophosphor of the marked region in Fig. 5(c) under an excitation wavelength of 980 nm. The obtained result reveals that the photoluminescence emission intensity is uniformly distributed in both $Gd_{1.8}(MoO_4)_3$:$Eu_{0.2}{}^{3+}$ downshift and $Gd_2(MoO_4)_3$:Er^{3+}/Yb^{3+} upconversion nanophosphors.

The $Gd_2(MoO_4)_3$:Eu^{3+} downshift nanophosphor can absorb photons of high energy in the range of 250–475 nm and give a strong red emission. The Si-solar cell cannot utilise photons
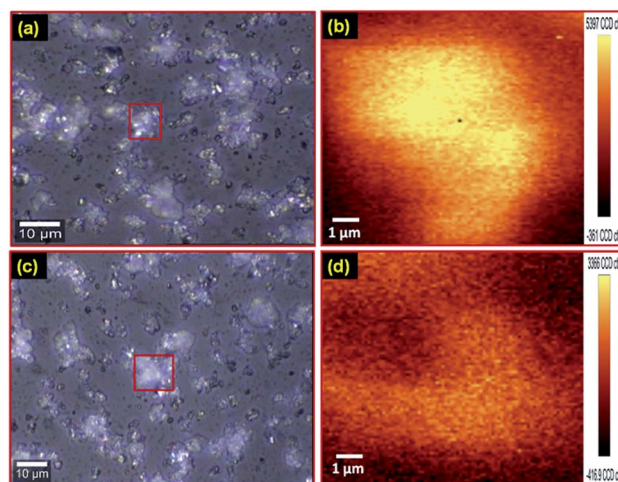

Fig. 5 (a) Optical image of the $Gd_{1.8}(MoO_4)_3$:$Eu_{0.2}{}^{3+}$ downshift nanophosphor on a glass slide, (b) the PL mapping image of the selected region (marked by red square in (a)) of the $Gd_{1.8}(MoO_4)_3$:$Eu_{0.2}{}^{3+}$ downshift nanophosphor excited at an excitation wavelength of 375 nm. (c) Optical image of the $Gd_2(MoO_4)_3$:Er^{3+}/Yb^{3+} upconversion nanophosphor on a glass slide, (d) the PL mapping image of the selected region (marked by red square in (c)) of the $Gd_2(MoO_4)_3$:Er^{3+}/Yb^{3+} upconversion nanophosphor excited at an excitation wavelength of 980 nm.

falling in this range of energy because of thermal losses. The $Gd_2(MoO_4)_3$:Eu^{3+} downshift nanophosphor can easily absorb the photons falling in this region and emits in the visible region

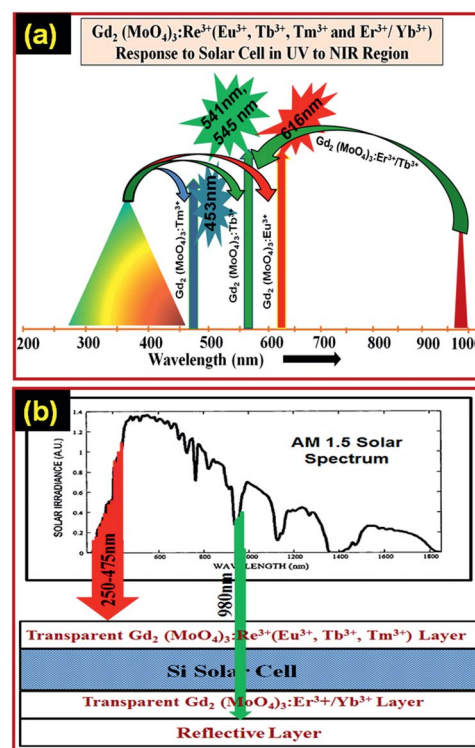Fig. 6 (a and b) Proposed schematic diagrams of the $Gd_2(MoO_4)_3$:Re^{3+} (Re^{3+} = Eu^{3+}, Tb^{3+}, Tm^{3+} and Er^{3+}/Yb^{3+}) nanophosphors (downshifts and upconversion) as a broad spectral converter from UV to NIR in order to enhance the efficiency of a Si-solar cell.

which can be easily absorbed by the Si-solar cell for electron–hole pair generation. The NIR region is also not absorbed by solar cells because for the NIR region solar cell is transparent. The $Gd_2(MoO_4)_3$:Er^{3+}/Yb^{3+} upconversion nanophosphor absorbs in the NIR region and emits in the visible region which can be easily absorbed by Si-solar cells. Therefore, the efficiency of the Si-solar cell could be enhanced by coating a thin layer of the downshift nanophosphor on the front side and an upconversion nanophosphor layer on the back side of the Si-solar cell. Fig. 6(a) and (b) illustrate a proposed spectral converter for $Gd_2(MoO_4)_3$:Re^{3+} (Re^{3+} = Eu^{3+}, Tb^{3+}, Tm^{3+} and Er^{3+}/Yb^{3+}) nanophosphors to enhance the efficiency of Si-solar cells. Thus, the obtained spectroscopy results reveal that the $Gd_2(MoO_4)_3$:Re^{3+} (Re^{3+} = Eu^{3+}, Tb^{3+}, Tm^{3+} and Er^{3+}/Yb^{3+}) nanophosphor could be a good choice as a spectral converter for upcoming next generation Si-solar cells.

4. Conclusions

We have successfully synthesized $Gd_2(MoO_4)_3$:Re^{3+} (Re^{3+} = Eu^{3+}, Tb^{3+} and Tm^{3+}) (downshift) and $Gd_2(MoO_4)_3$:Er^{3+}/Yb^{3+} (upconversion) nanophosphors by a customized solid state reaction method which can be easily scaled-up for large quantities. The structural and microstructure studies show that the nanophosphors have an orthorhombic crystal structure with an average size in the range of ~24–28 nm. $Gd_2(MoO_4)_3$ has an advantage over other host matrices as the excitation band is broad due to the charge transfer in O–Mo in the UV region, which sufficiently transfers energy to trivalent lanthanide ions. The $Gd_2(MoO_4)_3$:Eu^{3+} downshift nanophosphor demonstrates hypersensitive red emission at 616 nm corresponding to excitation in the range of 250–475 nm. The $Gd_2(MoO_4)_3$:Er^{3+}/Yb^{3+} upconversion nanophosphor shows strong green emission at 545 nm upon an excitation of 980 nm. The co-doping of Yb^{3+} ions assists the broad absorption in the NIR region as Yb^{3+} ions can absorb a broader range in the NIR region compared to Er^{3+} ions. Furthermore, the $Gd_2(MoO_4)_3$:Er^{3+}/Yb^{3+} upconversion nanophosphor demonstrates emission at 994 nm, which is rarely reported. Moreover, TRPL spectroscopy demonstrates a PL lifetime of $\tau_{av} \sim 0.64$ ms. Thus, the obtained PL and TRPL spectroscopy results of the synthesized nanophosphor legitimates its potential use as a broad spectral converter for next generation Si-solar cells.

Acknowledgements

References

1 G. D. Scholes, G. R. Fleming, A. Olaya-Castro and R. Grondelle, *Nat. Chem.*, 2011, **3**, 763–774.
2 N. S. Lewis and D. G. Nocera, *Proc. Natl. Acad. Sci. U. S. A.*, 2006, **103**, 15729–15735.
3 O. Morton, *Nature*, 2006, **443**, 19–22.
4 B. M. van der Ende, L. Aartsa and A. Meijerink, *Phys. Chem. Chem. Phys.*, 2009, **11**, 11081–11095.
5 X. Huang, S. Han, W. Huang and X. Liu, *Chem. Soc. Rev.*, 2013, **42**, 173–201.
6 A. J. Nozik and J. Miller, *Chem. Rev.*, 2010, **110**, 6443–6445.
7 H. A. Atwater and A. Polman, *Nat. Mater.*, 2010, **9**, 205–213.
8 P. K. Nayak, G. G. Belmonte, A. Kahn, J. Bisquert and D. Cahen, *Energy Environ. Sci.*, 2012, **5**, 6022–6039.
9 A. Goetzberger, C. Hebling and H. W. Schock, *Mater. Sci. Eng.*, 2003, **40**, 1–46.
10 B. van der Zwaan and A. Rabl, *Sol. Energ.*, 2003, **74**, 19–31.
11 B. S. Richards, *Sol. Energy Mater. Sol. Cells*, 2006, **90**, 2329–2337.
12 O. M. ten Kate, M. de Jong, H. T. Hintzen and E. van der Kolk, *J. Appl. Phys.*, 2013, **114**, 084502.
13 C. Strumpela, M. McCann, G. Beaucarne, V. Arkhipov, A. Slaoui, V. Svrcek, C. del Canizo and I. Tobias, *Sol. Energy Mater. Sol. Cells*, 2007, **91**, 238–249.
14 T. Trupke, M. A. Green and P. Würfel, *J. Appl. Phys.*, 2002, **92**, 4117.
15 H. Q. Wang, M. Batentschuk, A. Osvet, L. Pinna and C. J. Brabec, *Adv. Mater.*, 2011, **23**, 2675–2680.
16 S. F. H. Correia, V. de Z. Bermudez, S. J. L. Ribeiro, P. S. Andre, R. A. S. Ferreira and L. D. Carlos, *J. Mater. Chem. A*, 2014, **2**, 5580–5596.
17 W. Guo, K. Zheng, W. Xie, L. Sun, L. Shen, C. Liu, Y. He and Z. Zhang, *Sol. Energy Mater. Sol. Cells*, 2014, **124**, 126–132.
18 S. K. W. MacDougall, A. Ivaturi, J. Marques-Hueso, K. W. Krämer and B. S. Richards, *Sol. Energy Mater. Sol. Cells*, 2014, **128**, 18–26.
19 M. G. Debije and P. P. C. Verbunt, *Adv. Energy Mater.*, 2012, **2**, 12–35.
20 J. de Wild, A. Meijerink, J. K. Rath, W. G. J. H. M. van Sark and R. E. I. Schropp, *Energy Environ. Sci.*, 2011, **4**, 4835–4848.
21 E. Klampaftis, D. Ross, K. R. McIntosh and B. S. Richards, *Sol. Energy Mater. Sol. Cells*, 2009, **93**, 1182–1194.
22 W. G. J. H. M. van Sark, *Renewable Energy*, 2013, **49**, 207–210.
23 P. F. Scudo, L. Abbondanza, R. Fusco and L. Caccianotti, *Sol. Energy Mater. Sol. Cells*, 2010, **94**, 1241–1246.
24 X. Liu, L. Li, H. M. Noh, B. K. Moon, B. C. Choib and J. H. Jeong, *Dalton Trans.*, 2014, **43**, 8814–8825.
25 X. F. Liang, X. Y. Huang and Q. Y. Zhang, *J. Fluoresc.*, 2009, **19**, 285–289.
26 P. Kumar, J. Dwivedi and B. K. Gupta, *J. Mater. Chem. C*, 2014, **2**, 10468.
27 B. K. Gupta, D. Haranath, S. Saini, V. N. Singh and V. Shanker, *Nanotechnology*, 2010, **21**, 055607.
28 S. Abtmeyer, R. Pązik, R. J. Wiglusz, M. Małecka, G. A. Seisenbaeva and V. G. Kessler, *Inorg. Chem.*, 2014, **53**, 943–951.

29 A. Dwivedi, A. K. Singh and S. B. Rai, *Dalton Trans.*, 2014, **43**, 15906.

30 T. V. Gavrilovic, D. J. Jovanovic, V. Lojpur and M. D. Dramicanin, *Sci. Rep.*, 2014, **4**, 4209.

31 B. K. Gupta, N. N. Tharangattu, S. A. Vithayathil, Y. Lee, S. Koshy, A. L. M. Reddy, A. Saha, V. Shanker, V. N. Singh, B. A. Kaipparettu, A. A. Martí and P. M. Ajayan, *Small*, 2012, **8**, 3028–3034.

32 M. Haase and H. Schafer, *Angew. Chem., Int. Ed.*, 2011, **50**, 5808–5829.

33 A. Shalav, B. S. Richards, T. Trupke, K. W. Krämer and H. U. Güdel, *Appl. Phys. Lett.*, 2005, **86**, 013505.

34 D. Chen, L. Lei, A. Yang, Z. Wang and Y. Wang, *Chem. Commun.*, 2012, **48**, 5898–5900.

35 A. C. Pana, C. del Canizo, E. N. M. Santos, J. P. Leitao and A. Luque, *Sol. Energy Mater. Sol. Cells*, 2010, **94**, 1923–1926.

36 K. Mishra, S. K. Singh, A. K. Singh, M. Rai, B. K. Gupta and S. B. Rai, *Inorg. Chem.*, 2014, **53**, 9561–9569.

37 F. Lahoz, C. P. Rodrıguez, S. E. Hernandez, I. R. Martın, V. Lavın and U. R. R. Mendoza, *Sol. Energy Mater. Sol. Cells*, 2011, **95**, 1671–1677.

38 Y. Y. Cheng, B. Fuckel, R. W. MacQueen, T. Khoury, R. G. C. R. Clady, T. F. Schulze, N. J. E. Daukes, M. J. Crossley, B. Stannowski, K. Lips and T. W. Schmidt, *Energy Environ. Sci.*, 2012, **5**, 6953–6959.